Journal of Alloys and Compounds 509 (2011) 3822–3831

Contents lists available at ScienceDirect

Journal of Alloys and Compounds

journal homepage: www.elsevier.com/locate/jallcom

Phase relationships in the Al-rich region of the Al–Cu–Er system

Ligang Zhang[a,b,c,1], Patrick J. Masset[b], Fuyong Cao[a], Fangui Meng[d], Libin Liu[a,c,*], Zhanpeng Jin[a,c]

[a] School of Material Science and Engineering, Central South University, Lushan Street 105#, Changsha, Hunan 410083, PR China
[b] Freiberg University of Mining and Technology, Centre for Innovation Competence Virtuhcon, Fuchsmühlenweg 9, D-09596 Freiberg, Germany
[c] Science Center for Phase Diagram & Materials Design and Manufacture, Central South University, Changsha 410083, PR China
[d] School of Material Science and Engineering, Central South University of Forestry and Technology, Changsha, Hunan 410004, PR China

ARTICLE INFO

Article history:
Received 10 September 2010
Received in revised form 2 December 2010
Accepted 3 December 2010
Available online 10 December 2010

Keywords:
Al–Cu–Er system
Phase diagram
Solidification simulation
CALPHAD

ABSTRACT

The Al-rich region of the ternary Al–Cu–Er system is investigated using the method of X-ray diffraction, scanning electron microscopy with energy dispersive X-ray spectroscopy. Phase equilibria in the Al-rich region of the Al–Cu–Er system at 673 K have been obtained, and the microstructures of as-cast alloys in the Al-rich region are also investigated. One ternary phase τ_1-Al_8Cu_4Er with a composition of 59.4–60.4 at.% Al, 32.2–33.8 at.% Cu, and 6.4–7.7 at.% Er is observed in both as-cast and annealed alloys. At 673 K, the binary Al_3Er phase dissolves about 3.51 at.% Cu. The calculated solidification paths (based on the CALPHAD method) of as-cast alloys are in agreement with the experimental results.

1. Introduction

Interest in aluminum alloys is increasing continuously, especially for their potential applications in automotive and aerospace industries. Microalloying has been used to improve the high temperature strength of selected age hardenable Al alloys throughout the years [1–7]. Rare earth elements have been used in aluminum alloys for decades to improve the tensile strength, heat resistance and corrosion resistance, etc. [8–10]. For example, when Sc is added into Al alloys, a thermo-stable $L1_2$-type ($AuCu_3$) Al_3Sc phase will form in the Al solid solution, which can inhibit the re-crystallization and the grain growth and significantly improve the high temperature properties of the alloys [11–14]. Recently it has been shown that Er is also a favorable alloying element for aluminum alloys, especially in Al–Mg and Al–Cu alloys [15–19]. By increasing the proportion of Er, the as-cast grains are refined, the thermal stability of the alloy is improved, and the hardness and the strength are increased as well [20–25]. The reason of the above advantages is that the element Er can exist as Al3Er phase, which has a thermo-stable $L1_2$-type ($AuCu_3$) structure as Al_3Sc phase in aluminum based alloys and is capable to be coherent or semi-coherent with the Al matrix.

Only limited experimental information is available for this ternary system in the literature. The crystal structure data of solid phases in the Al-rich region have been previously assessed by Riani et al. [26], and listed in Table 1. Kuz'ma et al. have reported the isothermal section at 873 K [27]. On the base of these limited data, the thermodynamic parameters of the whole ternary Al–Cu–Er system have been assessed by present authors [28]. The purpose of the present work is to construct the isothermal sections at 673 K in the Al-rich region of Al–Cu–Er system experimentally and to verify the thermodynamic optimization of this ternary system.

2. Experimental

The Al–Cu–Er alloy samples were prepared from Al (99.9 wt.%), Cu (99.99 wt.%), Er (99.5 wt.%) metals and Al–10Er (wt.%) master alloy by arc-melting under argon. The ingots were re-melted five times to ensure their homogeneity. The weight loss detected after the arc-melting varied greatly with the alloy compositions (some alloys showed no weight loss at all). Ten samples with varied alloy compositions were selected to investigate the Al–Cu–Er ternary system, and their compositions are listed in Table 2. Among these alloys, seven samples were sealed in quartz tubes and isothermally annealed at temperature of 673 K for 40 days, then subsequently quenched in water.

Microstructures of the alloy samples were characterized using scanning electron microscopy (SEM) and energy dispersive spectrometry (EDS). SEM was performed with a FEI Sirion200 instrument operating in a backscattered electron (BSE) mode. And simultaneous EDS characterization was performed with an IXRF Systems instrument and software. Besides SEM–EDS, powder X-ray diffraction (XRD) data were collected with the Cu-K_α radiation on a Rigaku D/max 2550X X-ray diffractometer to identify specific phases in the produced alloys.

* Corresponding author at: School of Material Science and Engineering, Central South University, Lushan Street 105#, Changsha, Hunan 410083, PR China. Tel.: +86 073188877732; fax: +86 073188876692.
E-mail addresses: Ligang.Zhang@vtc.tu-freiberg.de (L. Zhang), PDC@mail.csu.edu.cn (L. Liu).
[1] Present address: Freiberg University of Mining and Technology, Centre for Innovation Competence Virtuhcon, Fuchsmühlenweg 9, D-09596 Freiberg, Germany.

0925-8388/$ – see front matter © 2010 Elsevier B.V. All rights reserved.
doi:10.1016/j.jallcom.2010.12.029

Table 1
Crystallographic data of intermetallic phases for Al-rich region of Al–Cu–Er system.

Phase	Lattice parameters[a]			Structure type, Pearson symbol, space group
	a (nm)	*b* (nm)	*c* (nm)	
θ	0.6067		0.4877	$CuAl_2$, *tI*12, *I*4/*mcm*
η	1.2066	0.4105	0.6913	CuAl, *mC*20, *C*2/*m*
$L1_2(Al_3Er)$	0.4214			$AuCu_3$, *cP*4, *Pm*3*m*
τ_1-Al_8Cu_4Er	0.8712		0.5130	$Mn_{12}Th$, *tI*26, *I*4/*mmm*

[a] The detection limit of the data for lattice parameter is within 0.0001 nm.

Table 2
Constituent phases and compositions of alloys.

Alloys	Nominal composition (at.%)			Heat-treatment	Phase identified
	Al	Cu	Er		
1#	95	3.3	1.7	673 K, 960 h	Fcc(Al) + τ_1-Al_8Cu_4Er + Al_3Er
2#	88	10.4	1.6	673 K, 960 h	Fcc(Al) + τ_1-Al_8Cu_4Er + θ
3#	81.8	16.7	1.5	673 K, 960 h	Fcc(Al) + τ_1-Al_8Cu_4Er + θ
4#	81.6	17.4	1	673 K, 960 h	Fcc(Al) + τ_1-Al_8Cu_4Er + θ
5#	76	22.7	1.3	673 K, 960 h	Fcc(Al) + τ_1-Al_8Cu_4Er + θ
6#	66	32.7	1.2	673 K, 960 h	τ_1-Al_8Cu_4Er + θ
7#	58	41	1	673 K, 960 h	τ_1-Al_8Cu_4Er + θ+η
8#	98.8	1	0.2	As-cast	Fcc(Al) + τ_1-Al_8Cu_4Er + θ
9#	98	1	1	As-cast	Fcc(Al) + τ_1-Al_8Cu_4Er + Al_3Er
10#	97.5	1	1.5	As-cast	Fcc(Al) + τ_1-Al_8Cu_4Er + Al_3Er

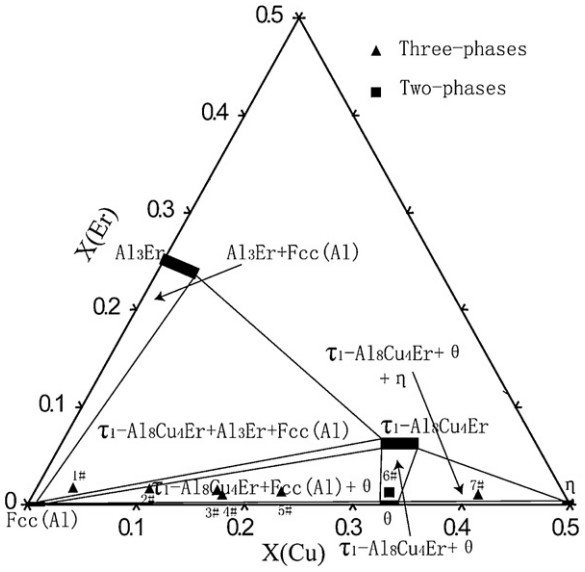

Fig. 1. Experimental isothermal section at 673 K in the Al–Cu–Er system (present work).

3. Results and discussion

3.1. The isothermal section at 673 K

The experimental investigation of the isothermal section at 673 K mainly focuses on the Al-rich region. Fig. 1 presents the phase relations determined after annealing the Al–Cu–Er alloys for up to 40 days. The solid lines are acquired according to the present measurement. The experimental information gained on the phase equilibra at 673 K is summarized in Table 3.

The ternary phase τ_1-Al_8Cu_4Er is proved to be stable at 673 K. According to the EDS results of alloys 1–7, the composition of τ_1-Al_8Cu_4Er is 59.4–60.4 at.% Al, 32.2–33.8 at.% Cu, and 6.4–7.7 Er. The measured composition is very close to the stoichiometric composition of Al_8Cu_4Er as it was reported previously [26–29].

In a good agreement with earlier studies [26], the solubility of Er in the binary θ and η phases was found to be very low. From Table 3, it is readily discernible that the Al_3Er phase dissolves up to 3.51 at.% Cu. It seems that Cu substitutes Al atoms on the Al sublattices of the Al_3Er phase since the measured Er composition does not change noticeably along the ternary extension of the Al_3Er phase.

Within the investigated composition ranges, 3 three-phase regions (Fcc(Al) + τ_1-Al_8Cu_4Er + Al_3Er, Fcc(Al) + τ_1-Al_8Cu_4Er + θ, τ_1-Al_8Cu_4Er + θ + η) and 1 two-phase region (τ_1-Al_8Cu_4Er + θ) are determined at 673 K in this work. The SEM micrographs and XRD patterns of alloy 1 annealed at 673 K for 40 days are shown in Fig. 2(a and b). As is shown in Fig. 2(a), the alloy (1#) consists of Fcc(Al), τ_1-Al_8Cu_4Er and Al_3Er phases, which is confirmed by its SEM micrograph (Fig. 2(b)) exhibiting a three-phases region (Fcc(Al) (dark) + τ_1-Al_8Cu_4Er (grey) + Al_3Er (white)). Meanwhile, the EDS results (as listed in Table 3) demonstrate that Al_3Er phase can dissolve up to 3.51 at.% Cu.

According to the SEM and XRD analyses, alloys 2–5 are located in the three-phases region (Fcc(Al) + τ_1-Al_8Cu_4Er + θ). Fig. 3(a) presents the XRD results of alloy 2, and its SEM micrograph is shown in Fig. 3(b), where the phases Fcc(Al) (dark), τ_1-Al_8Cu_4Er (white) + θ (grey) coexist in the microstructure.

Experimental results from XRD and SEM/EDS measurements carried out on alloy 6 are presented in Fig. 4(a and b). Based on these results, a two-phase region can be identified (τ_1-Al_8Cu_4Er + θ). In the alloy 7, a three-phase region (τ_1-Al_8Cu_4Er + θ + η) can be observed and has been already displayed in Fig. 5(a and b).

The determined phase relationships of Al-rich the region in Al–Cu–Er system are consistent with previous calculated results [28], as shown in Fig. 6 and Table 3. And the experimental and calculated phases and phase boundaries are compared in the Fig. 7, where the red lines indicate the experimental phase boundaries which are good agreement with the calculated ones (the black lines). The minor differences between experimental results and calculated ones are the phase regions of Al_3Er and τ_1-Al_8Cu_4Er, as is shown in Fig. 7, however, considering the experimental errors and the narrow ranges of solubility of these two phases, the deviations between calculated results and experiments are acceptable.

Table 3
Measured equilibrium alloy compositions and phases at 673 K for 40 days[a].

Alloys	Nominal composition (at. %)			Phase composition (at. %, EDX)			Phase identified	Phase field
	Al	Cu	Er	Al	Cu	Er		
1#	95	3.3	1.7	98.49	1.02	0.50	Fcc(Al)	Fcc(Al) + τ_1-Al_8Cu_4Er + Al_3Er
				61.09	32.56	6.35	τ_1-Al_8Cu_4Er	
				73.18	3.51	23.31	Al_3Er	
2#	88	10.4	1.6	97.99	1.52	0.49	Fcc(Al)	Fcc(Al) + τ_1-Al_8Cu_4Er + θ
				60.39	33.07	6.54	τ_1-Al_8Cu_4Er	
				66.37	33.63	0.00	θ	
3#	81.8	16.7	1.5	98.66	1.34	0.00	Fcc(Al)	Fcc(Al) + τ_1-Al_8Cu_4Er + θ
				59.76	33.78	7.56	τ_1-Al_8Cu_4Er	
				68.92	31.08	0.00	θ	
4#	81.6	17.4	1	98.36	1.52	0.12	Fcc(Al)	Fcc(Al) + τ_1-Al_8Cu_4Er + θ
				59.86	32.78	7.36	τ_1-Al_8Cu_4Er	
				66.83	32.30	0.87	θ	
5#	76	22.7	1.3	97.78	1.82	0.40	Fcc(Al)	Fcc(Al) + τ_1-Al_8Cu_4Er + θ
				60.17	32.16	7.67	τ_1-Al_8Cu_4Er	
				67.10	32.39	0.60	θ	
6#	66	32.7	1.2	60.39	33.07	6.54	τ_1-Al_8Cu_4Er	τ_1-Al_8Cu_4Er + θ
				66.37	33.63	0.00	θ	
7#	58	31	1	59.43	33.13	7.44	τ_1-Al_8Cu_4Er	τ_1-Al_8Cu_4Er + θ + η
				66.01	33.11	0.88	θ	
				48.11	51.08	0.81	η	

[a] The detection limit of the data for alloy composition is within 0.5 at.%

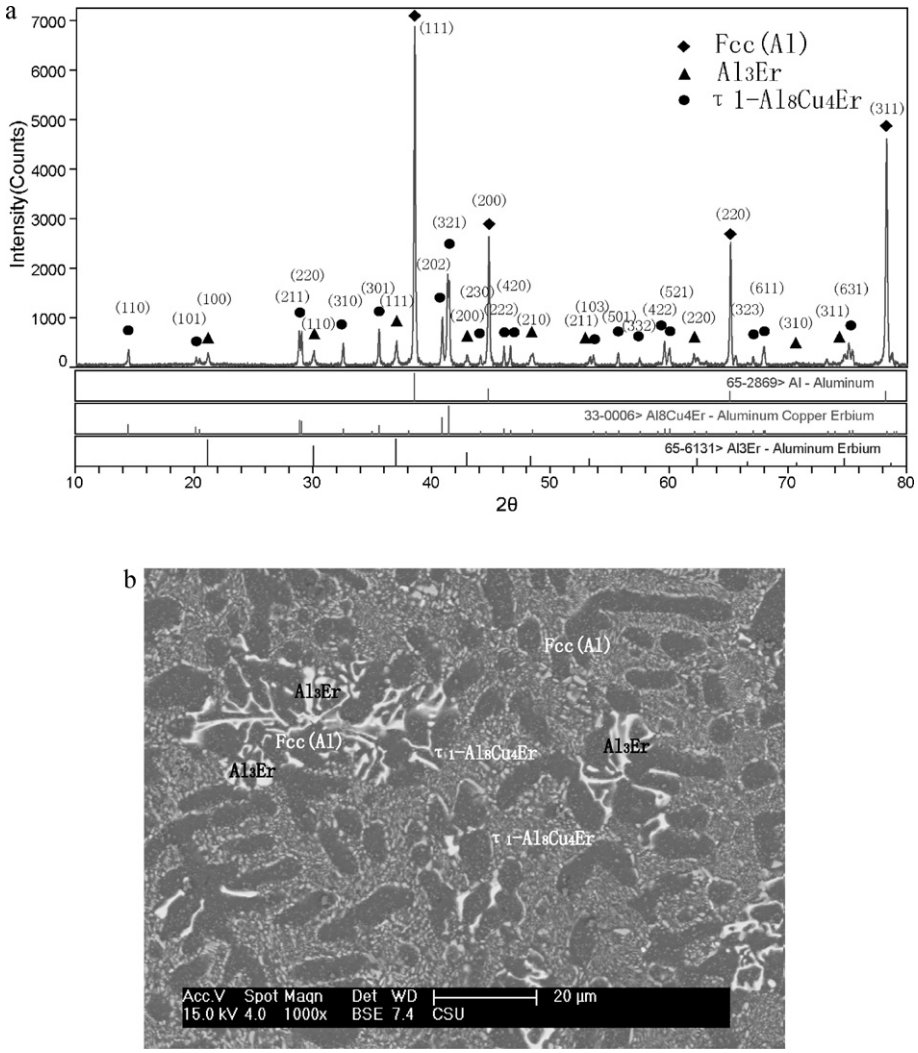

Fig. 2. Alloy 1 annealed at 673 K for 40 days. (a) XRD patterns of alloy 1; (b) micrograph of alloy 1 showing the co-existence of Fcc(Al) (black) + τ_1-Al_8Cu_4Er (grey) + Al_3Er (white).

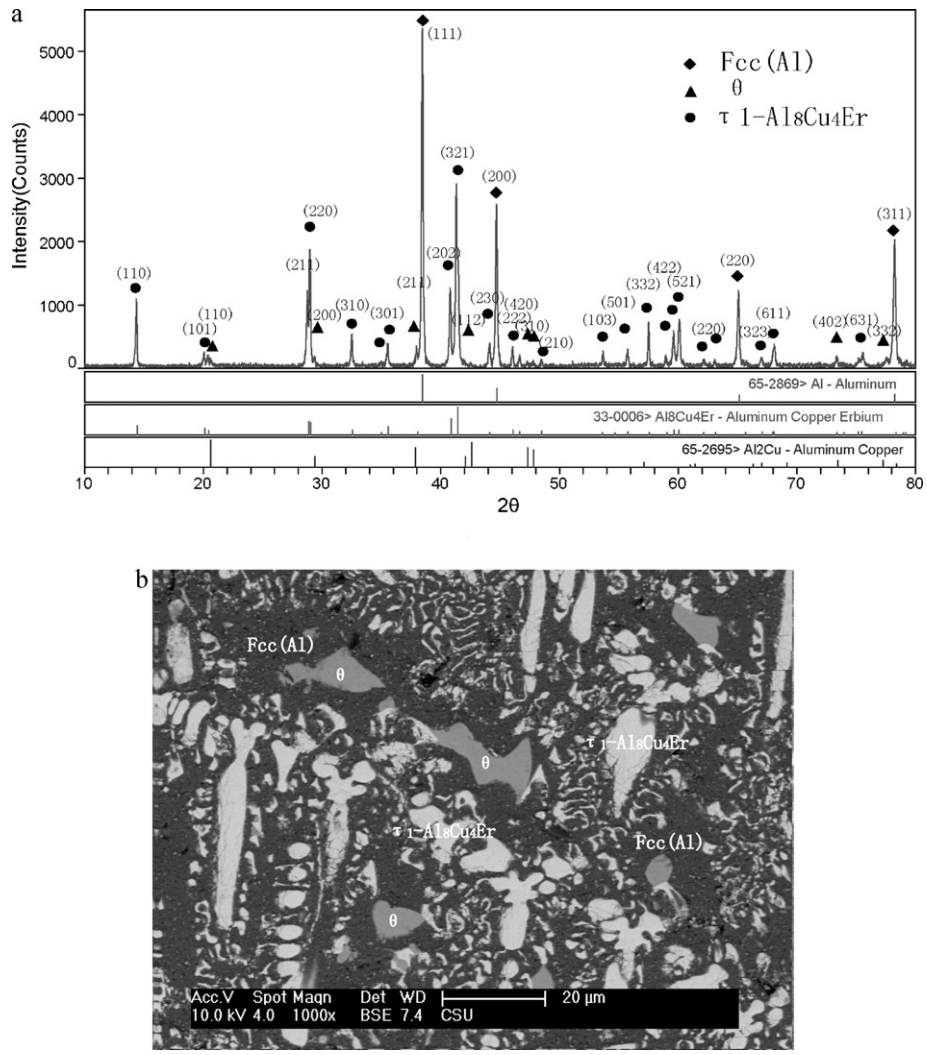

Fig. 3. Alloy 2 annealed at 673 K for 40 days. (a) XRD patterns of alloy 2; (b) micrograph of alloy 2 showing the co-existence of Fcc(Al) (black), τ_1-Al_8Cu_4Er (white) + θ (grey).

3.2. Microstructure of as-cast alloys

The as-cast alloy compositions are shown on the calculated Al-rich liquidus projection of Al–Cu–Er ternary system in Fig. 8. Solidification microstructures of these alloys are calculated based on thermodynamic database [28], as listed in Table 4.

Experimental results from XRD and SEM/EDS measurements on alloy 8 are presented in Fig. 9(a and b). Three phases (Fcc(Al) + τ_1-Al_8Cu_4Er + θ) are determined in this alloy, as is shown in Fig. 9(b). Fcc(Al) phase (dark one) corresponds to the primary crystal phase in this alloy. To confirm it, thermodynamic solidification simulations of alloy 8 under equilibrium and Scheil conditions [30] are conducted based on the results of Zhang et al. [28] with Pandat software [31], and the calculated results are shown in Figs. 10 and 11. Under both equilibrium and Scheil conditions, the Fcc(Al) phase is first formed from liquid (from point A_8 to B_8 in Fig. 10), subsequently an eutectic reaction (Liquid → Fcc(Al) + τ_1-Al_8Cu_4Er) occurs (point B_8). In equilibrium condition, the solidification of alloy 8 should ends at such eutectic reaction. While under Scheil's condition, excess liquid react with τ_1-Al_8Cu_4Er phase after the eutectic reaction, following a peri-eutectic reaction (liquid + τ_1-Al_8Cu_4Er → Fcc(Al) + θ). The peri-eutectic reaction (liquid + τ_1-Al_8Cu_4Er → Fcc(Al) + θ) fails to happen completely due to the high cooling rate and the remaining liquid phase solid-

Table 4
Microstructures of as-cast alloys comparing with calculated results.

Alloys	Nominal composition (at.%)			Condition	Calculated results [21]	Phase identified
	Al	Cu	Er			
8#s	98.8	1	0.2	Equilibrium	Fcc(Al) + τ_1-Al_8Cu_4Er	Fcc(Al) + τ_1-Al_8Cu_4Er + θ
				Scheil	Fcc(Al) + τ_1-Al_8Cu_4Er + θ	
9#	98	1	1	Equilibrium	Fcc(Al) + Al_3Er + τ_1-Al_8Cu_4Er	Fcc(Al) + Al_3Er + τ_1-Al_8Cu_4Er
				Scheil	Fcc(Al) + Al_3Er + τ_1-Al_8Cu_4Er	
10#	97.5	1	1.5	Equilibrium	Fcc(Al) + Al_3Er + τ_1-Al_8Cu_4Er	Fcc(Al) + Al_3Er + τ_1-Al_8Cu_4Er
				Scheil	Fcc(Al) + Al_3Er + τ_1-Al_8Cu_4Er	

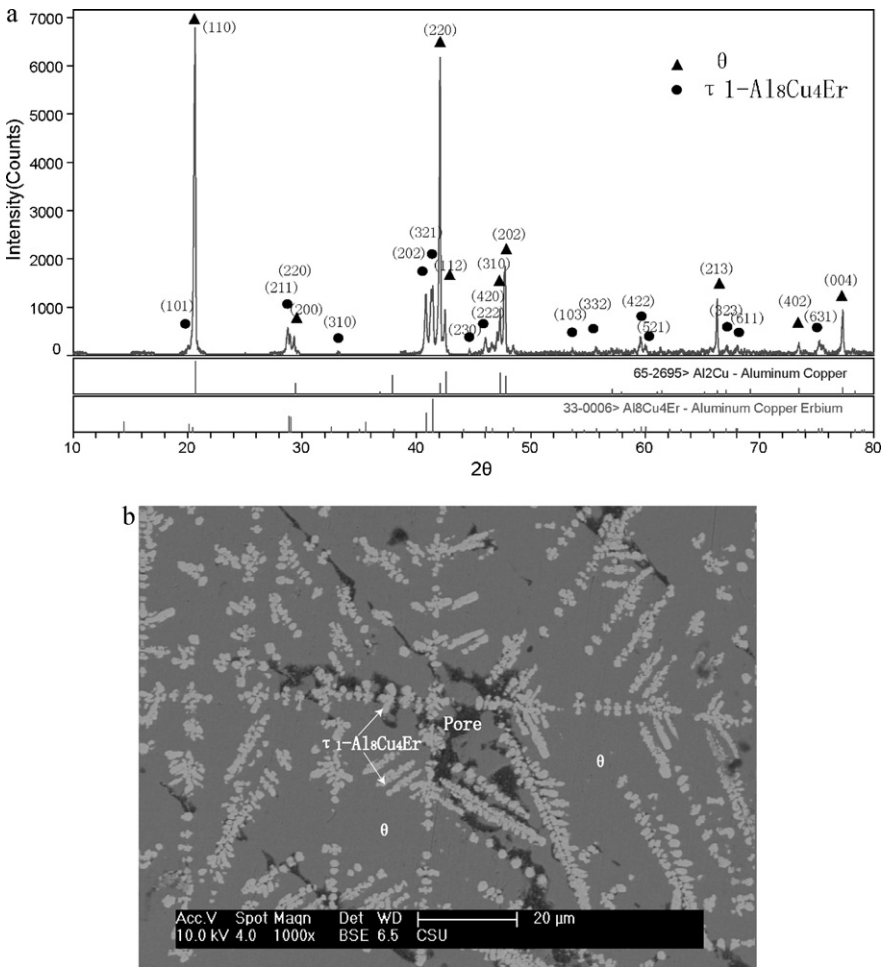

Fig. 4. Alloy 6 annealed at 673 K for 40 days. (a) XRD patterns of alloy 6; (b) micrograph of alloy 6 showing the co-existence of τ_1-Al_8Cu_4Er (white) + θ (grey).

ify after the eutectic reaction (liquid → Fcc(Al) + θ). Finally, the excess liquid react completely during this eutectic reaction (liquid → Fcc(Al) + θ) under this non-equilibrium condition (Scheil). From above discussion, we can draw a conclusion that the solidification simulation under Scheil condition is more consistent with experimental results, as we can find Fcc(Al) + θ eutectic structure in Fig. 9.

Experimental results from XRD and SEM/EDS measurements on the alloys 9 and 10 are presented in Figs. 12 and 14, respectively. Three phases (Fcc(Al) + τ_1-Al_8Cu_4Er + Al_3Er) are determined in these alloys, as is shown in Figs. 12(a) and 14(a). Based on thermodynamic calculations using the database of Al–Cu–Er ternary system [16], solidification paths of alloys 9 and 10 under equilibrium and Scheil conditions are calculated. In the forming process of these alloys Fcc(Al) phase first precipitates from the liquid alloy, and it is followed by the eutectic reaction (liquid → Fcc(Al) + τ_1-Al_8Cu_4Er) with temperature decreasing, ending up with a ternary eutectic reaction (liquid → Fcc(Al) + τ_1-Al_8Cu_4Er + Al_3Er) under equilibrium and scheil conditions, as is shown in Figs. 13 and 15. The experimental microstructures (ternary eutectic microstructure in Figs. 12(b) and 14(b)) of alloys 9–10 are in good agreement with the calculated solidification paths, as shown in Figs. 13 and 15. Moreover, comparing Figs. 12(b) with 14(b), it can be found that the amounts of ternary eutectic microstructures in the alloy 10 are more than that in the alloy 9. The reason is that the alloy composition of the alloy 10 is more close to the ternary eutectic point compared with that of the alloy 9, which is shown in the calculated liquidus projection (Fig. 8).

Based on the above information, the observed microstructures vary significantly with the alloy compositions and solidification conditions. These differences can be explained by thermodynamic calculation using the CALPHAD method. The thermodynamic database can therefore be considered to be a solid working basis for designing Al alloys.

4. Summary

The phase relationships for the Al-rich region of Al–Cu–Er ternary system at 673 K were determined by X-ray diffraction, scanning electron microscopy with energy dispersive X-ray spectroscopy. Three three-phase regions (Fcc(Al) + τ_1-Al_8Cu_4Er + Al_3Er, Fcc(Al) + τ_1-Al_8Cu_4Er + θ, τ_1-Al_8Cu_4Er + θ + η) and one two-phase region (τ_1-Al_8Cu_4Er + θ) were confirmed at 673 K in this work. The measured phase relationships of the Al–Cu–Er system at 673 K are consistent with thermodynamic calculations using the CALPHAD method. Experimental microstructures of Al-rich as-cast alloys were also investigated, and are consistent with thermodynamic solidification prediction based on the CALPHAD method. And the resulting thermodynamic database was applied to case studies of as-cast alloys, showing that the literature thermodynamic description of the Al–Cu–Er system is reliable as a working basis for computer-assisted alloy design.

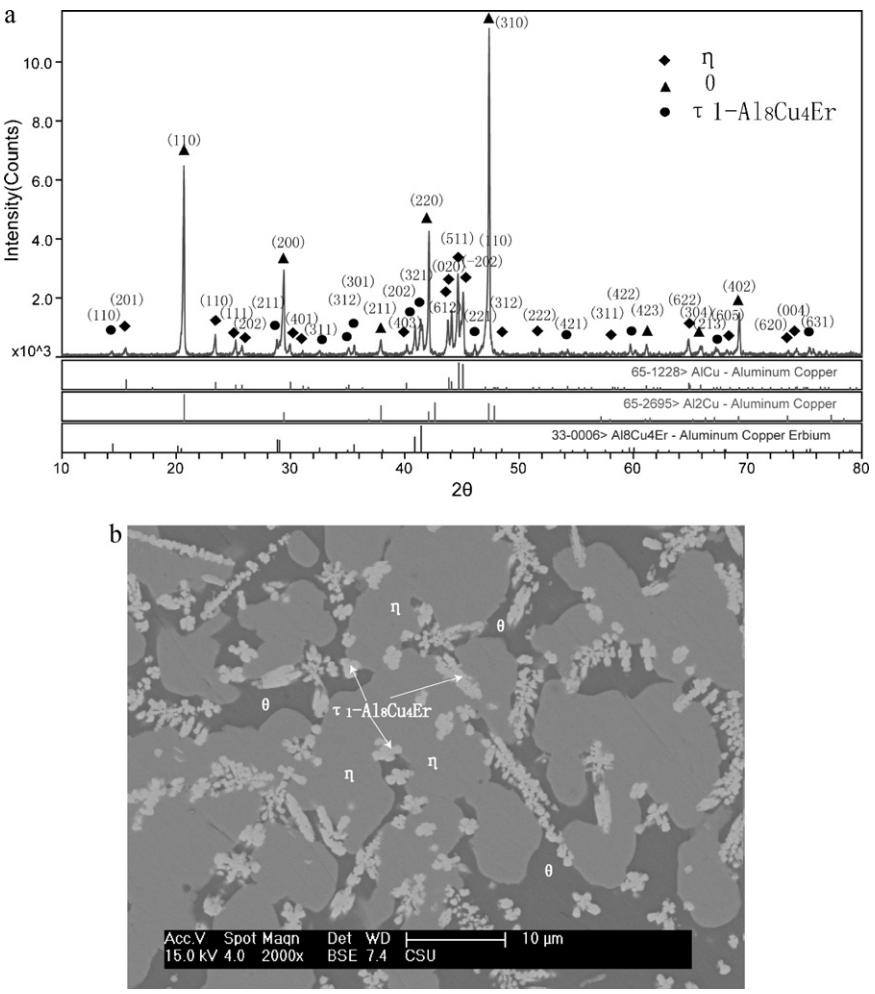

Fig. 5. Alloy 7 annealed at 673 K for 40 days. (a) XRD patterns of alloy 7; (b) micrograph of alloy 7 showing the co-existence of τ_1-Al_8Cu_4Er (white) + θ (black) + η (grey).

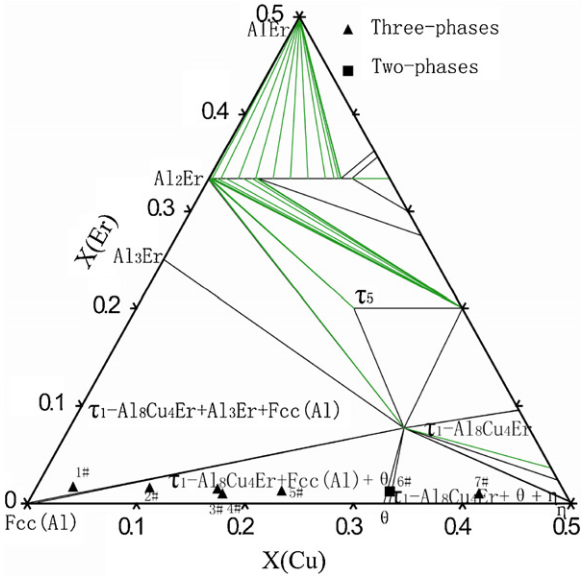

Fig. 6. The calculated isotherm section of Al–Cu–Er system at 673 K [21] with experimental alloys.

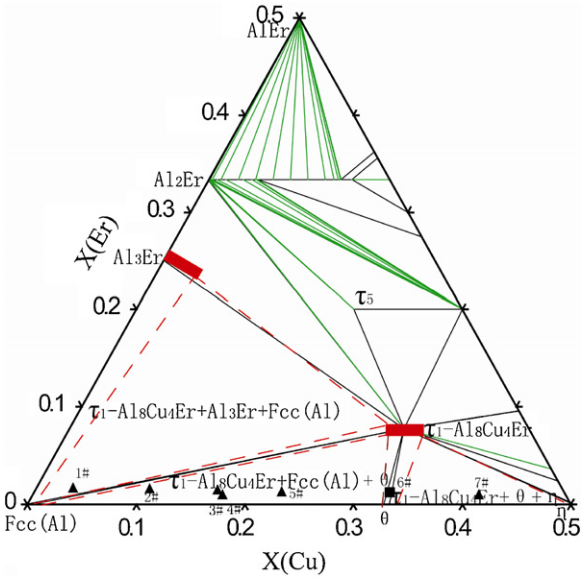

Fig. 7. The calculated isotherm section of Al–Cu–Er system at 673 K compared with experimental information. Note red lines indicate the measured phases relationships including terminal compositions; black lines are the calculated phase equilibria; green lines are the calculated tie-lines. (For interpretation of the references to color in this figure legend, the reader is referred to the web version of the article.)

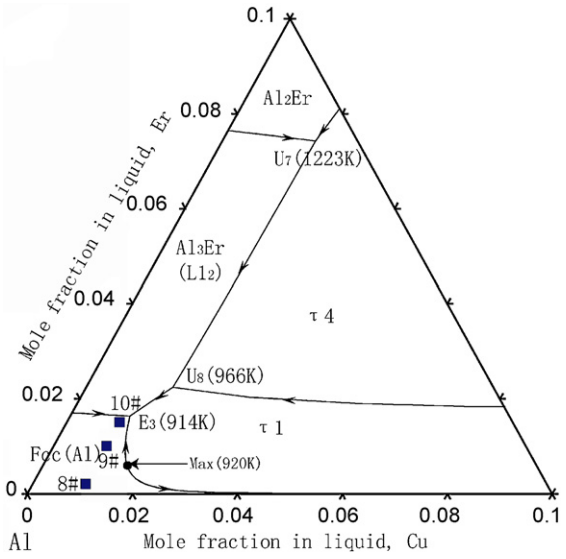

Fig. 8. The calculated liquidus projection of Al-rich side with alloy compositions.

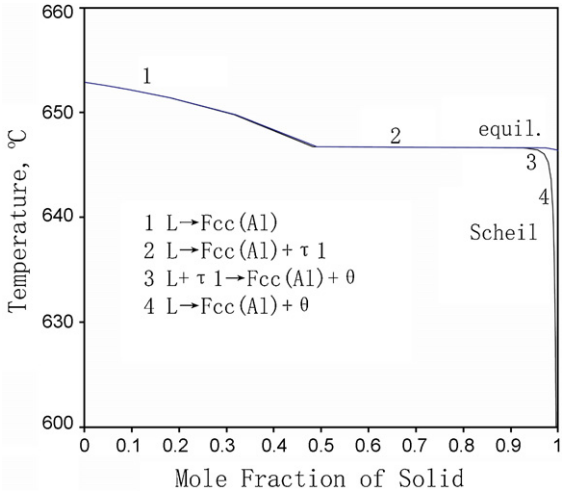

Fig. 10. Calculated solid phase fraction for alloy 8 under the equilibrium and Scheil conditions with temperature change.

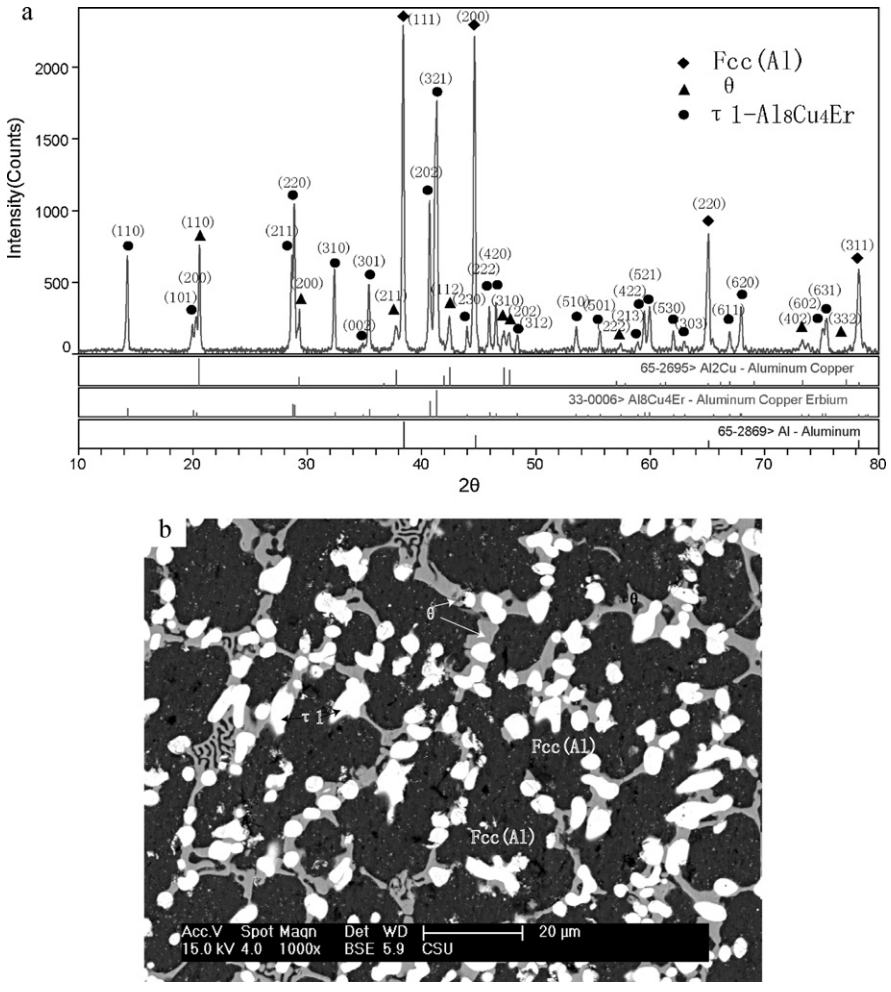

Fig. 9. Microstructure of as-cast alloy 8. (a) XRD patterns of alloy 8; (b) micrograph of alloy 8, phases τ_1-Al_8Cu_4Er (white), θ (grey), and Fcc(Al) (black).

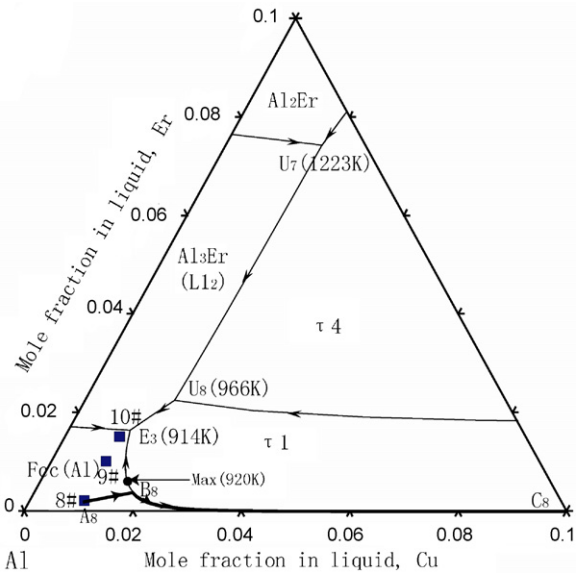

Fig. 11. The calculated solidification path of alloy 8 under Scheil condition.

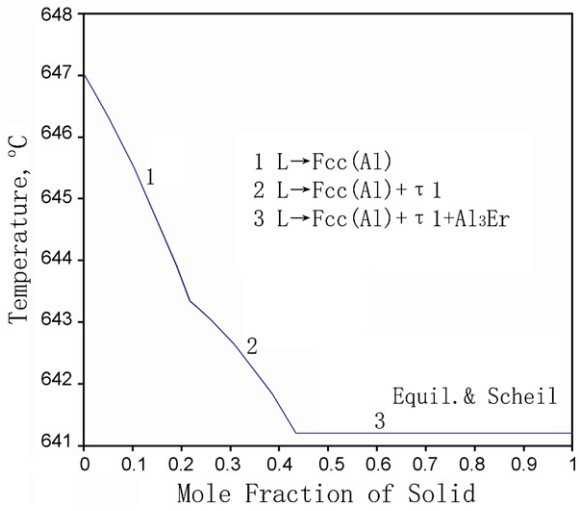

Fig. 13. Calculated solid phase fraction for alloy 9 under the equilibrium and Scheil conditions with temperature change.

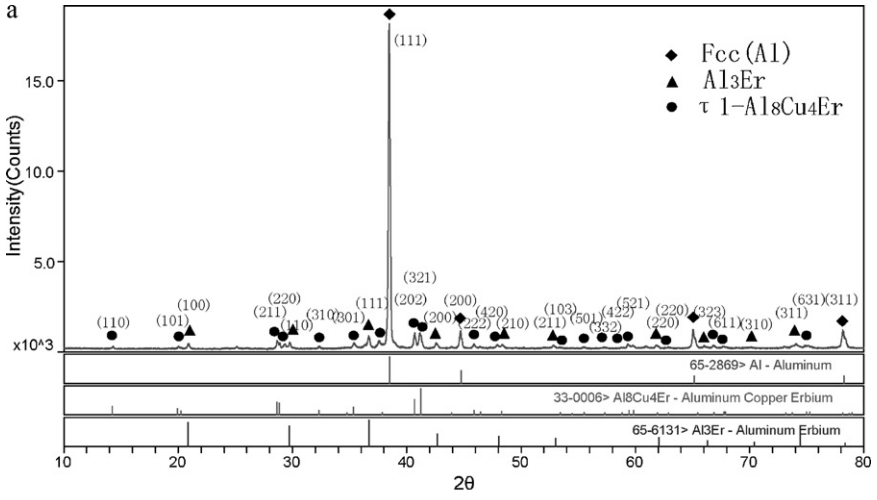

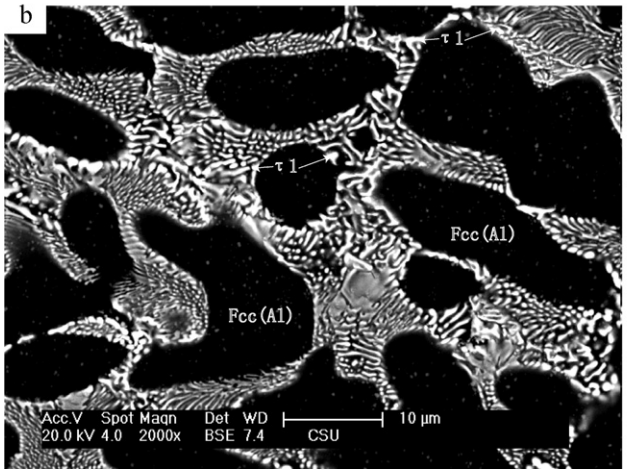

Fig. 12. Microstructure of as-cast alloy 9. (a) XRD patterns of alloy 9; (b) micrograph of alloy 9, phases τ_1-Al_8Cu_4Er (white) and Fcc(Al) (black).

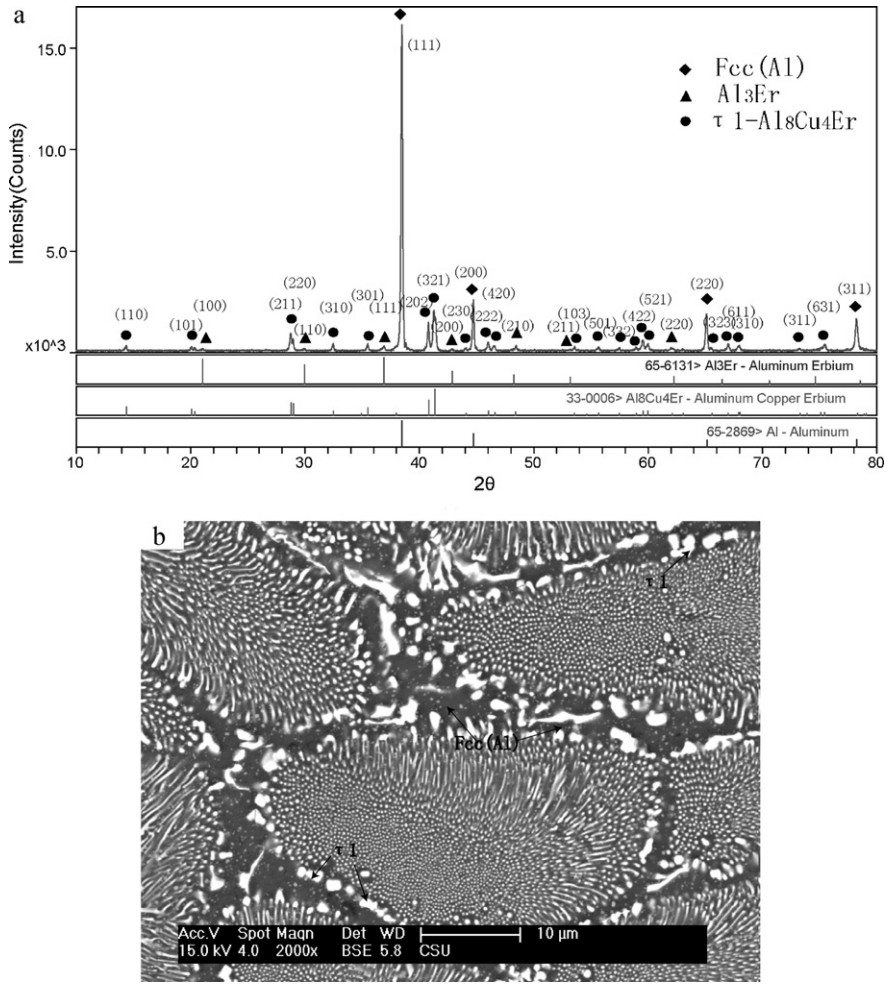

Fig. 14. Microstructure of as-cast alloy 10. (a) XRD patterns of alloy 10; (b) micrograph of alloy 10, phases τ_1-Al_8Cu_4Er (white) and Fcc(Al) (black).

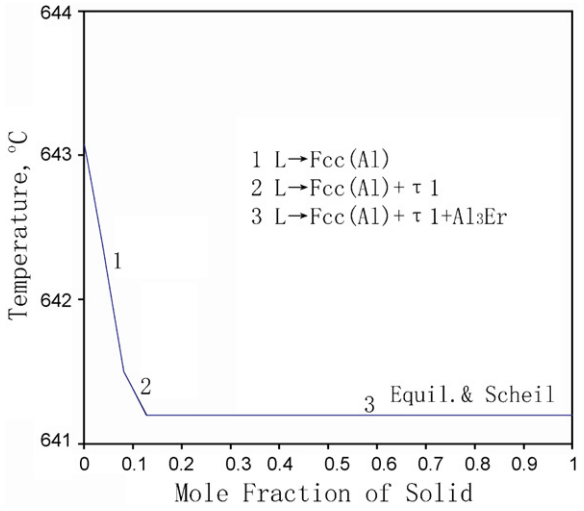

Fig. 15. Calculated solid phase fraction for alloy 10 under the equilibrium and Scheil conditions with temperature change.

Acknowledgments

This work is financially supported by National Science Foundation of China (grant nos. 50771106, 50971136 and 50731002), Key Project of Chinese Ministry of Education (no. 109122), Project of excellent doctor degree of Central South University (no. 2008yb014) and the Scientific Research Foundation of Hunan Province Department of Land & Resources, China (2008K 22). Thermodynamic calculations are performed using the Pandat program licensed from The CompuThermo, LLC, Madison, WI, USA.

References

[1] N. Tabatabaei, A. Karimi, M. Vaseghi, J. Alloys Compd. 502 (2010) 59–62.
[2] C.H. Fan, Z.H. Chen, W.Q. He, J.H. Chen, D. Chen, J. Alloys Compd. 504 (2010) L42–L45.
[3] S. Bai, Z.Y. Liu, Y.T. Li, Y.H. Hou, X. Chen, Mater. Sci. Eng. A 527 (2009) 1806–1814.
[4] B. Klobes, O. Balarisi, M. Liu, T.E.M. Staab, K. Maier, Acta Mater. 58 (2010) 6379–6384.
[5] X.Y. Liu, Q.L. Pan, X. Fan, Y.B. He, W.B. Li, W.J. Liang, J. Alloys Compd. 484 (2009) 790–794.
[6] H. Bo, S. Jin, L.G. Zhang, X.M. Chen, H.M. Chen, L.B. Liu, F. Zheng, Z.P. Jin, J. Alloys Compd. 484 (2009) 286–295.
[7] L.G. Zhang, X.M. Chen, H.Q. Dong, J. Shan, L.B. Liu, F. Zheng, Z.P. Jin, J. Alloys Compd. 480 (2009) 403–408.
[8] F. Rosalbino, E. Angelini, S. De Negri, A. Saccone, S. Delfino, Intermetallics 11 (2003) 435–441.
[9] W.T. Wang, X.M. Zhang, Z.G. Gao, Y.Z. Jia, L.Y. Ye, D.W. Zheng, L. Liu, J. Alloys Compd. 491 (2010) 366–371.
[10] H. Bo, L.B. Liu, Z.P. Jin, J. Alloys Compd. 490 (2010) 318–325.
[11] A.F. Norman, K. Hyde, F. Costello, S. Thompson, S. Birley, P.B. Prangnell, Mater. Sci. Eng. A 354 (2003) 188–198.
[12] W. Lefebvre, F. Danoix, H. Hallem, B. Forbord, A. Bostel, K. Marthinsen, J. Alloys Compd. 470 (2009) 107–110.
[13] W.J. Kim, J.K. Kim, H.K. Kim, J.W. Park, Y.H. Jeong, J. Alloys Compd. 450 (2008) 222–228.
[14] W.S. Lee, T.H. Chen, C.F. Lin, M.S. Chen, J. Alloys Compd. 493 (2010) 580–589.
[15] L.G. Zhang, L.B. Liu, G.X. Huang, B.R. Jia, Trans. Nonferrous Met. Soc. China (17) (2007) S16–20.
[16] M. Fass, D. Itzhak, D. Eliezer, F.H. Froes, J. Mater. Sci. Lett. 6 (1987) 1227–1228.

[17] X. Chen, Z.Y. Liu, S. Bai, Y. Li, L.H. Lin, J. Alloys Compd. 505 (2010) 201–205.
[18] T. Yanson, M. Manyako, O. Bodak, R. Cerny, K. Yvon, J. Alloys Compd. 320 (2001) 108–113.
[19] Z.L. Yang, Y.Z. Zhan, H.L. Mo, Y. Du, H.H. Xu, J. Alloys Compd. 503 (2001) 61–64.
[20] Z.N. Nie, T.N. Jin, G.F. Xu, Patent CN 01134612.4, 2001-11-17.
[21] R. Ferro, A. Saccone, G. Borzone, J. Rare Earths 15 (1997) 45–61.
[22] F. Rosalbino, E. Angelini, S. De Negri, A. Saccone, S. Delfino, Intermetallics (13) (2005) 55–60.
[23] D.H. Xiao, J.N. Wang, D.Y. Ding, Mater. Sci. Technol. 20 (2004) 1237–1240.
[24] R.A. Karneskya, D.C. Dunanda, D.N. Seidman, Acta Mater. 14 (2009) 4022–4031.
[25] Z.R. Nie, J.B. Fu, J.X. Zou, T.N. Jin, J.J. Yang, G.F. Xu, H.Q. Ruan, T.Y. Zuo, Mater. Forum 28 (2004) 197–201.
[26] P. Riani, L. Arrighi, R. Marazza, D. Mazzone, G. Zanicchi, R. Ferro, J. Phase Equilibr. 25 (2004) 22–52.
[27] Y.B. Kuz'ma, T.V. Pan'kiv, Izv. Akad. Nauk SSSR, Metally 3 (1989) 218–219.
[28] L.G. Zhang, L.B. Liu, G.X. Huang, H.Y. Qi, B.R. Jia, Z.P. Jin, CALPHAD 32 (2008) 527–534.
[29] V. Raghavan, J. Phase Equilibr. 31 (2010) 285–287.
[30] E. Scheil, Z. Metallkde 34 (1942) 70–72.
[31] PANDAT Software for Multicomponent Phase Diagram Calculations by CompuTherm, LLC, Madison, WI, since 2000.